Geophysical Journal International

Geophys. J. Int. (2026) **245,** 1–15
Advance Access publication 2026 January 15
Research Paper

https://doi.org/10.1093/gji/ggag017

Rayleigh-wave focal spot imaging of the European Alps and surrounding areas

C. Tsarsitalidou,[1] G. Hillers,[1] L. Stehly,[2] B. Giammarinaro,[3] P. Boué[2] and A. Paul[2]

[1]*Institute of Seismology, University of Helsinki,* 00014 *Helsinki, Finland. E-mail: christina.tsarsitalidou@helsinki.fi*
[2]*Institut des Sciences de la Terre, Grenoble Alpes University,* 38058 *Grenoble, France*
[3]*LabTAU, INSERM, Centre Léon Bérard, University Lyon* 1, 69424 *Lyon, France*

Accepted 2026 January 5. Received 2025 December 22; in original form 2025 August 8

SUMMARY

We apply Rayleigh-wave focal spot imaging to seismic records collected by ∼800 stations in the European Alps and surrounding areas and demonstrate the effectiveness of the method for lithospheric imaging in a complex plate boundary environment. We reconstruct ZZ-component focal spots from AlpArray and related network data and estimate fundamental-mode Rayleigh-wave phase velocities in the 20 to 200 s period range using spatial autocorrelation (SPAC) models. Using a short data distance on the order of 1λ allows us to study Rayleigh waves at longer periods compared to the limits of ambient-noise tomography. We implement SPAC models corrected for the anisotropic background illumination to mitigate the observed strong surface-wave energy incidence in the SW-NE direction. The comparison between our focal spot imaging results and two regional tomography studies demonstrates the resolution power of the method for non-isotropic wavefield conditions and a spatially variable array shape. We invert the Rayleigh-wave dispersion curves using the Neighbourhood Algorithm to construct a pseudo 3-D shear-wave velocity model between 20 and 200 km depth and to image the Moho topography. The agreement of the obtained velocity features with reference shear-wave models illustrates the potential of focal spot imaging to resolve relevant structural information and helps to establish the local time domain spatial autocorrelation analysis as a complementary approach to ambient-noise tomography.

Key words: Crustal imaging; Seismic interferometry; Seismic noise; Surface waves and free oscillations.

1 INTRODUCTION

Seismic imaging using scattered or diffuse wavefields has developed into a mature approach for the characterization of Earth structure at near-surface and crustal scale. The emergence of seismic interferometry together with the availability of affordable seismic sensors (S.J. Arrowsmith *et al.* 2022) has led to the extension and development of established and new passive dense-array imaging techniques (D. Draganov *et al.* 2009; F.C. Lin *et al.* 2009; G. Ekström *et al.* 2009; F.C. Lin & M.H. Ritzwoller 2011; E. Galetti & A. Curtis 2012; P. Poli *et al.* 2012; N. Nakata *et al.* 2015; S.A.L. de Ridder & B.L. Biondi 2015; G. Hillers *et al.* 2016; T. Blondel *et al.* 2018; J. Wang *et al.* 2019; Y. Lu *et al.* 2020) that can produce high-resolution images of complex subsurface structures.

The passive dense-array surface-wave focal spot imaging method estimates medium properties locally. The focal spot is the large-amplitude feature at lag time $\tau = 0$ s of the 2-D noise correlation wavefield centred on a reference station considered as the virtual source. It can be understood to result from the refocusing of far-field propagating waves on the source. In passive seismology the surface wave refocusing is reconstructed from the cross-correlations of the ambient-noise field, which is equivalent to active ultrasound time-reversal experiments (M. Fink 1999; A. Derode *et al.* 2003a, b). The narrowband zero-lag cross-correlation amplitude distribution is the time domain spatial autocorrelation and thus equivalent to the frequency-domain spatial autocorrelation or SPAC (K. Aki 1957). We use this equivalence (V.C. Tsai & M.P. Moschetti 2010) and parametrize the focal spot with the models developed for the SPAC method (K. Aki 1957; H. Okada & K. Suto 2003) and its extension (M.M. Haney *et al.* 2012) to estimate fundamental mode Rayleigh-wave phase velocity c_R (G. Hillers *et al.* 2016; B. Giammarinaro *et al.* 2023; C. Tsarsitalidou *et al.* 2024).

Focal spot imaging uses the SPAC formulae and related theoretical developments (H. Nakahara 2006), notably the

$J_0(\omega r/c_R)$ parametrization of the vertical Rayleigh-wave component, where J_0 denotes the Bessel function of order zero, and the parameters in the argument are the angular frequency, the distance and the phase velocity. The focal spot dense array approach differs from typical SPAC applications in geotechnical engineering. In contrast to the triangular or circular SPAC arrays (S. Foti *et al.* 2018), modern dense seismic arrays share acquisition similarities with ultrasound transducers and their dense spatial sampling used in passive elastography. Seismic focal spot imaging adopts the elastography focal spot approach (S. Catheline *et al.* 2013; J. Brum *et al.* 2015) and compiles images without solving a tomographic inverse problem by iteratively estimating the local phase velocity from the time-domain spatial autocorrelation field using frequency-filtered data from short distances r (G. Hillers *et al.* 2016; C. Tsarsitalidou *et al.* 2024). This differs from the dense-array SPAC applications by G. Ekström (2014) and E.D. Kästle *et al.* (2018) that invert for $c(\omega)$ dispersion curves from propagating signals between station pairs followed by a phase velocity tomography at each frequency ω. Numerical focal spot experiments showed that the velocity can be robustly estimated using data from distances in the range of 1λ from the centre station, with strong implications for an improved lateral resolution (B. Giammarinaro *et al.* 2024). Super resolution can potentially be achieved when the focal spot reconstruction has a high signal-to-noise ratio (SNR), which is further facilitated by a high station density in a subarray (C. Zemzemi *et al.* 2020). Moreover, the absence of a minimum interstation distance cutoff, typically set at 2λ (chapter 5, N. Nakata *et al.* 2019), allows an analysis of wavelengths that are long compared to tomography, which extends the depth resolution of seismic surface-wave focal spot imaging (B. Giammarinaro *et al.* 2023). This was demonstrated in the first large-scale USArray focal spot application (C. Tsarsitalidou *et al.* 2024) that extended Rayleigh-wave phase velocity imaging to 310 s period compared to the tomography 150 s limit (K. Zhao *et al.* 2017). These strong advantages are balanced by a sensitivity of the focal spot shape to imperfect surface wavefields including interfering body wave components, that can, however, be mitigated using longer data ranges r, at the expense of a decreased resolution (R. Takagi *et al.* 2014; B. Giammarinaro *et al.* 2023; C. Tsarsitalidou *et al.* 2024).

Following the USArray application (C. Tsarsitalidou *et al.* 2024), we here apply the focal spot imaging to continuous data recorded by stations in the European Alps and the Italian Peninsula to estimate the fundamental mode Rayleigh-wave phase velocity in the 20 to 200 s period range. Seismic images based on data of the national permanent networks of the Alpine states and the adjacent countries constrained the complicated velocity structure in this tectonically complex plate boundary region. The deployment of the temporary AlpArray network in 2015 (AlpArray Seismic Network 2015) increased the resolution of seismic images significantly. AlpArray data have been facilitating a wide range of ambient-noise imaging approaches (A. Paul *et al.* 2024, and references therein). They underpin improvements of the first ambient-noise surface wave tomography (L. Stehly *et al.* 2009) that now show high-resolution images of the European crust and upper-mantle structure and the subduction of the European crust under the Adria microplate (A. Nouibat *et al.* 2023). Y. Lu *et al.* (2018) and A. Nouibat *et al.* (2022) constructed group velocity images up to 150 s period using a 2-D linearized and transdimensional inversion, respectively, of Rayleigh-wave traveltime data exploring ray paths from stations in continental Europe and the UK. E.D. Kästle *et al.* (2018) estimated Rayleigh-wave phase velocities between 4 and 250 s by applying the SPAC implementation of G. Ekström (2014) to noise cross-correlations up to 75 s and the two-station method to earthquake data for the longer periods.

Compared to the USArray application (C. Tsarsitalidou *et al.* 2024), here we use an updated focal spot analysis to better mitigate biasing effects associated with the directional surface-wave energy flux. In this AlpArray analysis too the focal spot imaging results are compatible with tomographic reference models, which again supports the effectiveness of the local imaging approach. The average interstation distance is with 50 km comparable to the USArray, however, we find that the stronger small-scale lateral velocity variations associated with the plate collision together with the irregular array shape influence the imaging results in ways that highlight the potential of further processing improvements. Here we invert the local focal spot dispersion curves for the first time to compile a pseudo-3-D shear-wave velocity (v_S) model. Our focus is to explore the potential of constraining v_S estimates from focal spot dispersion curves, which are directly derived from the spatial autocorrelations and thus subject to measurement uncertainties that are not regularized or averaged during a tomographic inversion process. We discuss our imaging results but do not aim to produce an updated v_S model that can supersede established shear-wave models.

In Section 2 we introduce the AlpArray data set, and we describe the signal processing and the updated focal spot dispersion analysis. In Section 3 we describe the Rayleigh-wave dispersion curve inversion. In Section 4.1 we discuss the obtained phase velocity results in comparison to tomography results (E.D. Kästle *et al.* 2018; A. El-Sharkawy *et al.* 2020), before we show the v_S structure and the Moho topography in Sections 4.2 and 4.3, respectively. We emphasize the good agreement with tomography at the short periods, and the challenges posed by the imaging configuration at long periods.

2 FOCAL SPOT IMAGING

2.1 Data selection, pre-processing and noise correlations

We use vertical component, continuous records of about 800 stations deployed across the European Alps, its surroundings and the Italian peninsula, between 3°−19° E and 36°−50° N. Together with the permanent stations in the area, we include stations of the temporary AlpArray (AlpArray Seismic Network 2015) and the two line arrays Cifalps (L. Zhao *et al.* 2016) and Cifalps2 (L. Zhao *et al.* 2018) in the Western Alps. We exclude stations from the EASI network in the Eastern Alps (AlpArray Seismic Network 2014) because of the obtained poor quality on the velocity estimation. We use the AlpArray land-based stations deployed in the Greater Alpine region that were operating between two to four years. The average interstation distance is 50 km.

Ambient-noise cross-correlations provide an estimate of the Green's function assuming a sufficiently scattered wavefield or homogeneously distributed noise sources (M. Campillo & P. Roux 2015). However, many data applications indicate localized

and persistent excitation patterns that result in spatially variable ambient-noise wavefield properties. Time and frequency-domain normalization of the ambient-noise records can help to mitigate biasing effects in cross-correlations that result from non-stationarity (G.D. Bensen *et al.* 2007). Focal spot imaging can use the same signal processing chain that is used in ambient-noise tomography. We implement the same processing as in the USArray focal spot application (C. Tsarsitalidou *et al.* 2024). We apply a low-pass filter, decimate the daily records to 1 Hz, remove the instrument response and apply a bandpass filter in the 2.2−400 s range. For every 4 hr segment, the amplitude is normalized in the frequency domain using spectral whitening and clipped in the time domain at three times the standard deviation of the amplitude distribution in that window.

We compute 4 hr time-window cross-correlations to obtain the vertical–vertical (ZZ) component of the Green's tensor. While ZZ-component focal spots can consist of Rayleigh surface-wave and body-wave energy, they exhibit significantly higher SNR compared to tensor elements involving the radial component, and allow overall more robust velocity estimates (C. Tsarsitalidou *et al.* 2024). The maximum correlation lag time $\tau = 1000$ s facilitates the frequency filtering of the correlation wavefield up to 200 s period. We normalize the cross-correlations with the energy of both traces and apply a linear stack. For the Rayleigh-wave phase velocity estimates we apply a narrowband Gaussian filter to each cross-correlation defined as $h(\omega) = e^{-\alpha(\frac{\omega-\omega_c}{\omega_c})^2}$, where $\alpha = 1000$ and ω_c is the central angular frequency of the Fourier transform of the cross-correlation (B. Giammarinaro *et al.* 2023). The filter targets periods between 20 and 200 s in increments of 10 s. Before filtering, we zero-pad the correlations to increase the period sampling for better resolution of the target filter periods.

2.2 Isotropic focal spot parametrization

The steps of data pre-processing and the computation of cross-correlations for tomography and focal spot imaging applications are the same. However, the two approaches differ in the correlation-field analysis for the estimation of the phase velocity and the reconstruction of dispersion curves. Focal spot imaging does not yield group or phase velocity images that involve the regularization of the observed velocity variations in a 2-D tomographic inversion. We estimate local dispersion curves at each station location through the SPAC Bessel-function model parametrization. This is similar to the ESPAC method (H. Okada & K. Suto 2003), which has been, however, mainly applied to geotechnical surveys using small-scale arrays composed of a few sensors (M.W. Asten & K. Hayashi 2018).

In classic SPAC applications a complete azimuthal data average around the reference station provides accurate velocity estimates even in the case of strong anisotropic or even plane-wave incidence. Again, the focal spot is the time-domain spatial autocorrelation that is equivalent to the zero-lag time cross-correlation amplitude distribution, and it forms a Fourier transform pair with the frequency-domain spatial autocorrelation wavefield (V.C. Tsai & M.P. Moschetti 2010). This relation was used in the first focal spot imaging applications (G. Hillers *et al.* 2016; C. Tsarsitalidou *et al.* 2024), where the zero-lag amplitudes $A(r)$ of the ZZ-component cross-correlations were parametrized using the classic 1-D SPAC result

$$A(r, \tau = 0) = \sigma J_0(kr) \tag{1}$$

to estimate the fundamental mode Rayleigh-wave phase velocity $c_R = \omega/k$, with k denoting the wavenumber. The amplitude scaling factor σ accounts for the Rayleigh-wave power and pre-processing effects (G. Hillers *et al.* 2016). Importantly, the data range r is on the order of the wavelength λ, and the choice of r can trade-off the SNR-dependent precision of average velocities and the spatial resolution of medium heterogeneity (B. Giammarinaro *et al.* 2024).

2.3 Anisotropic AlpArray focal spots and model regression

The uneven coverage of noise sources affects the focal spot shape, as observed in Fig. 1(a) for periods of 50, 100 and 200 s. The focal spots are not circular, and the images indicate a stronger incidence in the SW-NE direction that is parallel to the shortened focal spot axis (B. Giammarinaro *et al.* 2023). This incidence is compatible with sea wave model predictions of seismic hum generation for the periods above 50 s along the European West coast (F. Ardhuin *et al.* 2015; M. Deen *et al.* 2018). The implementation of the isotropic SPAC formula (eq. 1) provides accurate velocity estimates when the focal spot is fully reconstructed at all azimuths (K. Aki 1957; B. Giammarinaro *et al.* 2023). It is expected that the phase velocity uncertainties are larger for non-optimal imaging configurations, for example, along the edge of the array or when the focal spot has the same scale as the array aperture (C. Tsarsitalidou *et al.* 2022). To limit the effects of potentially biasing configurations associated with the spatially variable AlpArray deployment we use a SPAC parametrization that is adapted to the observed background illumination.

Sub-vertically incident *P*-wave energy excited by ocean-solid earth interactions and reverberations associated with large earthquakes (P. Boué *et al.* 2014) interfere at zero-lag time with the refocusing Rayleigh waves (C. Tsarsitalidou *et al.* 2024). In this AlpArray pilot application we do not analyse the surface and body wave partitioning in more detail (C. Tsarsitalidou *et al.* 2024). We fit the Bessel-function model to focal spot data using a conservative data or regression distance of $r_{\text{fit}} = 1.5\lambda$. This choice is based on numerical and observational results (B. Giammarinaro *et al.* 2023; C. Tsarsitalidou *et al.* 2024) that show that the biasing effect of *P*-wave energy decreases significantly using regression distances larger than 1λ.

The cross-correlation tensor for anisotropic incidence has been derived for scalar (H. Cox 1973; H. Nakahara 2006) and vector waves (M.M. Haney *et al.* 2012; R. Takagi *et al.* 2014). Most SPAC and the previous focal spot applications use the isotropic model discussed in Section 2.2. Our AlpArray analysis is the first large-scale data application that considers the wavefield anisotropy in the 2-D regression model. This model is based on the expression for the spatial autocorrelation coefficient developed by M.M. Haney *et al.* (2012)

$$C(r, \psi) = a_0 J_0(kr) + \sum_{m=1}^{M-1} j^m J_m(kr)\big(a_m \cos(m\psi) + b_m \sin(m\psi)\big), \tag{2}$$

where the a_m and b_m are weights, j is the imaginary unit, ψ is the azimuthal angle between the reference station at the origin and a target station, and J_m is a Bessel function of the first kind of the order of m. The summation is performed over $m = 0$—which

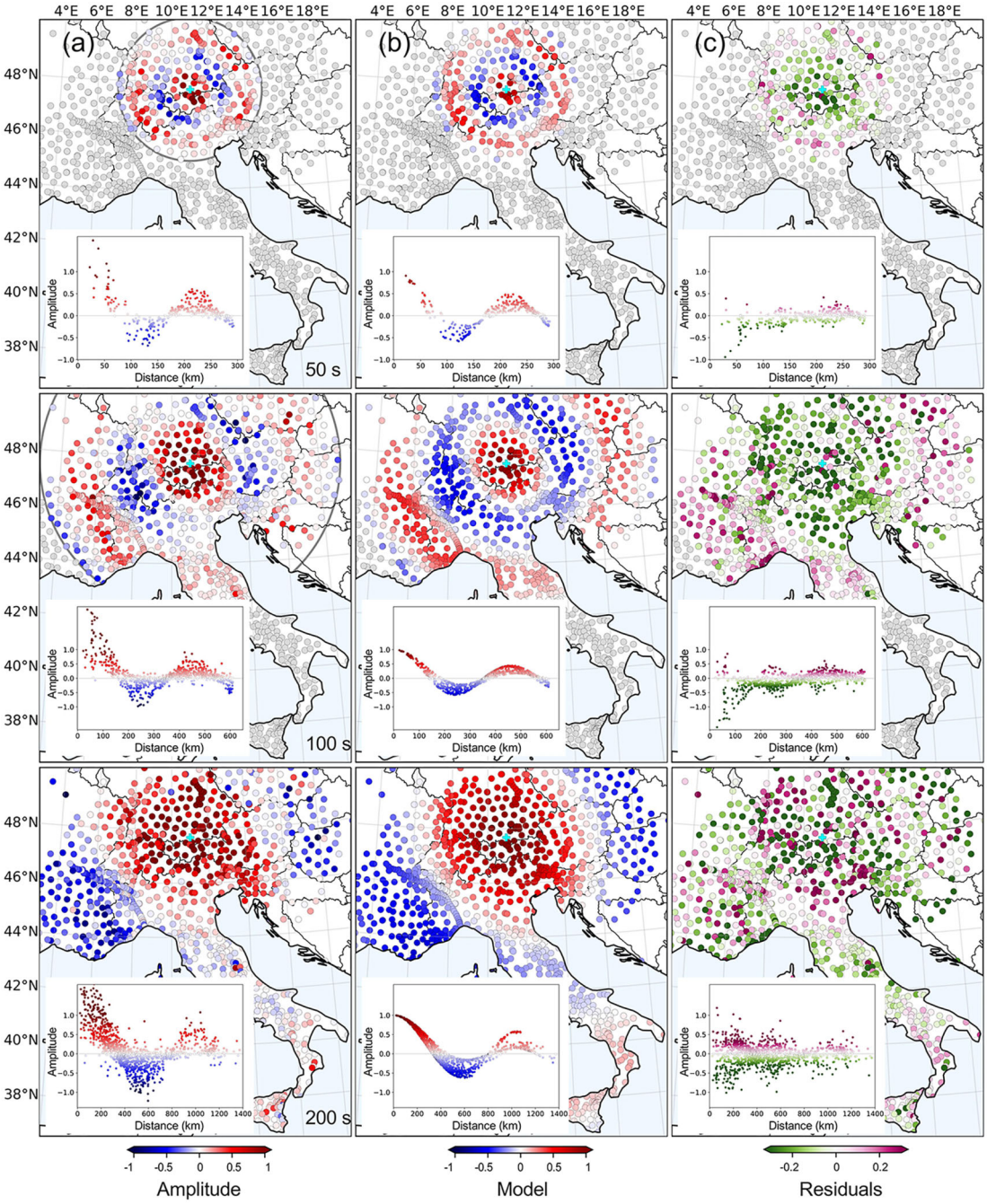

Figure 1. (a) ZZ-component narrowband filtered focal spots at periods of 50, 100 and 200 s for the station Z3A143A, indicated as cyan-colored cross. (b) The model amplitude after fitting the focal spot data from panel (a) using the anisotropic regression described in Section 2.3. (c) Difference between the model in panel (b) and the focal spot data in panel (a). Data from stations indicated in grey are not used in the regression. The grey circle indicates the data range used for the velocity estimation. The insets show the amplitude distributions as a function of distance. The line array across the French-Italian border is the Cifalps2 line.

includes the a_0 weight—and $M-1$ where M denotes the number of the correction terms, which depends on the wavenumber k and the data range r_{fit} (L. Seydoux *et al.* 2017). In our time-domain focal spot parametrization, only the real part of eq. (2) is used. The number of correction terms in the summation is always $M = 9$, because r_{fit} is a function of the wavelength λ. Here, $M = k_{\text{ang}} r_{\text{fit}} = \frac{2\pi}{\lambda} 1.5\lambda \approx 9.4$, where k_{ang} is the angular wavenumber. To parametrize the focal spots and estimate the isotropic Rayleigh-wave phase velocity from narrowband zero-lag ZZ-component cross-correlation amplitude data eq. (2) becomes

$$\begin{aligned} A(r, \psi, \tau = 0) = \sigma J_0(kr) - J_2(kr)\big(a_2 \cos(2\psi) + b_2 \sin(2\psi)\big) \\ + J_4(kr)\big(a_4 \cos(4\psi) + b_4 \sin(4\psi)\big) \\ - J_6(kr)\big(a_6 \cos(6\psi) + b_6 \sin(6\psi)\big) \\ + J_8(kr)\big(a_8 \cos(8\psi) + b_8 \sin(8\psi)\big). \end{aligned} \quad (3)$$

For a given period or frequency, the free parameters are the Bessel-function argument wavenumber k that is equivalent to the target phase velocity c_R, the amplitude factor σ and the weights $a_2, b_2, \ldots, a_8, b_8$.

The phase velocity is estimated by an iterative procedure similar to the isotropic approach used by C. Tsarsitalidou *et al.* (2024). We perform a nonlinear regression of the Gaussian filtered focal spot data three times to estimate the free parameters k, σ and the a_m and b_m weights. The difference is that we use eq. (3) for the second and third iteration that accounts for the effects of the anisotropic background illumination on the noncircular focal spot shapes.

During the first iteration, the focal spot regression is performed using the isotropic SPAC formula (eq. 1) with no distance restriction and with free parameters k_1 and σ_1. At this point, k_1 is estimated to determine the data range r_{fit} for the next two iterations. We perform the second iteration by fitting the model in eq. (3) to focal spot data from distances up to $r_{\text{fit}} = 1.5\lambda$, with $M = k_1 r_{\text{fit}}$. At this second step, the free parameters are k_2 and σ_2—the indices denote the second iteration—and the weights $a_{2,4,6,8}$ and $b_{2,4,6,8}$. We scale the focal spot data with σ_2 and fit the data again with the anisotropic model. Scaling with the factor σ ensures properly normalized residual sum of squares RSS estimates that are computed from the misfit between the focal spot data and the Bessel-function model. While the shape of the residual distribution is not affected by the scaling, the value range is. We do not update the wavenumber estimate from the second to the third step, that is, $k_2 = k_3$, however, after the third iteration σ_3 equals unity.

Figs 1(b) and (c) show the model and the residuals between the focal spot model and data (Fig. 1a) after the third iteration of the regression, respectively, for the periods 50, 100 and 200 s. The insets in Figs 1(a), (b) and (c) show the azimuthally independent 1-D focal spot, the model and residuals as a function of distance. Overall, the obtained 2-D models in Fig. 1(b) have a similar elliptical shape as the observed focal spots with a shortened axis in the SW-NE direction. The corresponding 1-D model distributions illustrate how the anisotropic incidence influences the radial amplitude variations at a given distance. Compared to these models the data in the insets in Fig. 1(a) exhibit a significant variability at very short distances that indicate an overall poor SNR that decreases with period. The difference between the model and the focal spot data is plotted in Fig. 1(c). The greener colours around the origin at 50 and 100 s indicate larger observed compared to modelled amplitudes. In the 1-D representation we can observe an overall asymptotic behaviour to neutral residuals at larger distances, a trend that decreases with increasing period. This is compatible with a consistent sinc-function component associated with coherent body-wave energy (H. Cox 1973) that is not parametrized by the Rayleigh-wave focal spot model. Towards longer periods this asymptotic component decreases and the scattering indicative of a poor SNR dominates the pattern. The envelope of the residuals exhibits the shape of two opposite oscillating functions. That is, focal spot samples are lower and higher compared to the model at the same distance, and this trend is stronger between the zero crossings. This implies that the first-order effects are associated with the target surface-wave behaviour that controls the azimuthally dependent zero crossings.

The iterative regression estimates the period-dependent phase velocity and the associated RSS quality control parameter. From the RSS we can further estimate the standard error (R.C. Aster *et al.* 2013),

$$\varepsilon_k = \sqrt{\frac{\text{RSS}}{\text{dof}} \cdot C_k}, \tag{4}$$

where C_k is the diagonal element of the parameter covariance matrix for the wavenumber k and dof indicates the degrees of freedom, that is, the number of data points minus the number of free parameters, which is 10 for an order number 8. The Rayleigh-wave phase velocity error ε_{c_R} is then computed using standard error propagation concepts.

2.4 Focal spot phase velocity images

We apply a range of narrowband Gaussian filters (Section 2.1) to estimate Rayleigh-wave dispersion for the 20 to 200 s period range. We compile spatial distributions of the period-dependent phase velocity, RSS and the error by assigning each estimate to the location of the associated station. The Voronoi tessellation of the obtained images (Section 4.1) mirrors the station locations and preserves the information of the array properties, highlighting the dense-array imaging character of the focal spot method. On each period-dependent phase velocity image we perform a quality control to remove outliers that we find are more frequent compared to the USArray results (C. Tsarsitalidou *et al.* 2024). For this we use the interquartile range IQR of the corresponding RSS and the phase velocity distributions. For each period, we keep dispersion measurements that fall within the $Q1-1.5$ IQR and $Q3+1.5$ IQR range in each image, where $Q1$ and $Q3$ denote the first and third quartiles of the estimated velocity distributions, respectively. We also remove dispersion measurements associated with RSS values higher than the $Q3+1.5$ IQR of the RSS distribution. These thresholds were empirically chosen to yield more cohesive images. This period-dependent quality control can lead to local dispersion curves composed of a varying number of samples. We exclude stations from the EASI network (AlpArray Seismic Network 2014) because of the observed consistent low-quality results. On the other hand, the results along the Cifalps and Cifalps2 (L. Zhao *et al.* 2016, 2018) line arrays are compatible with the nearby observations, that is, the linear array shape does not show in the velocity distributions, but the decreased signal-to-noise ratio associated with different deployment times can be indicated in the associated standard error maps. This implies that the dense instrumentation along a specific direction relative to the background illumination does not negatively affect the obtained regression results.

To further eliminate remaining outliers, that is, small-scale artefacts that are not compatible with the results in the neighbouring locations, we apply a median filter. For each period, the phase velocity value at each station is replaced by the median of the phase velocities from that station and its two nearest neighbours. This low-pass filtering works well for our irregular, nonuniform grid with its variable interstation distances. We find that velocity estimates tend to be more robust in regions with high station density, leading to higher resolution that may be compromised by an alternative fixed-distance filtering. We discuss the obtained results and compare them with published phase velocity maps in Section 4.1. Considering that spatial filtering was not applied in the USArray focal spot application that used a shorter $r_{\text{fit}} = 1.2\lambda$ for the image production stage, our AlpArray

analysis implies a more challenging imaging environment that can be attributed to the combination of greater structural complexity, topography variations and the irregular array geometry.

3 INVERSION OF RAYLEIGH-WAVE DISPERSION CURVES

We invert each Rayleigh-wave dispersion curve between 20 and 200 s period for 1-D shear-wave velocity v_S profiles to compile a pseudo 3-D v_S model. Each inversion is a stochastic direct search performed by the Neighbourhood Algorithm NA (M. Sambridge 1999). Using the NA, the model space is explored randomly and non-uniformly towards areas of low misfit, as new sample models are created based on the performance of tested models. The model space is created from *a priori* parameter ranges of the layer v_S values and the interface depths between layers of constant velocity. Solutions for v_P and density ρ are not explored in the inversion but are constrained by empirical laws in relation to v_S.

Our objective is to investigate if local v_S profiles can be constrained by inverting focal spot dispersion curves, and to assess to what degree the resulting 3-D images can be related to the known structure of the target region. The examples in Figs 2(a) and S1 show that the blue indicated dispersion curves derived from the focal spot data tend to be less smooth compared to results typically obtained from ambient-noise tomography. However, we show below that the NA yields robust v_S models that are compatible with reference results from tomography applications that employ different inversion algorithms (A. Nouibat *et al.* 2022; E.D. Kästle *et al.* 2025). Table 1 summarizes the model space parameters used for the inversion. The choice of the parameters is based on initial inversion tests limited to the area between 7°−12° E and 44°−48° N. While a pre-defined parametrization may cause potentially resolvable layers near the parameter bounds to be missed, it can also stabilize the inversion and accelerate convergence. We explore four layers between 10 and 270 km depth. Rayleigh waves with periods of 20 s and longer have a weak sensitivity at shallow depths. For the topmost 10 km we fix the v_S value using the model by A. Nouibat *et al.* (2023) with no exploration.

At the first step of each inversion, 300 000 models are randomly explored. Every model is used to compute a theoretical dispersion curve (R.B. Herrmann 2013), and the comparison to the observation yields a misfit value. We estimate the misfit as $m = \sum \mathrm{m}_i \mathrm{d}f$, where m_i is the difference between the synthetic and observed dispersion measurement i normalized by the standard error of the velocity estimation, and $\mathrm{d}f$ is the difference between adjacent frequency samples assuming continuous misfit measurements along the frequency axis. We keep the 1000 best models and test 100 more models in their neighbourhood by computing again synthetic dispersion curves and estimating their misfit. This step is iterated ten times. For the inversion of each dispersion curve we explore 1300 000 models. From these models we compile a posterior $v_S(z)$ distribution, which allows us to quantify the probability of occurrence of a particular v_S value and interface across the considered depth range. The probability distributions are obtained by discretizing the $v_S(z)$ distributions using bins of 1 km and 50 m s^{-1} and add the misfit dependent weight $e^{-0.5m}$ of each model to this distribution.

Fig. 2 shows an example of the inversion for the station CH.BOURR located in the Swiss Jura mountains. The observed dispersion curve (Fig. 2a) has been obtained using the spatial median filter applied at each period. Error bars at each period indicate the uncertainty. The synthetic dispersion curve associated with the weighted average of the 500 best models is shown in orange. The obtained dispersion curves exhibit sample-by-sample variations that are not modelled by the synthetic dispersion curves [e.g. Fig. S1(b), (c) and (e) at 130 s]. These fluctuations result from the narrow Gaussian filter and the spatial discretization that signifies the focal spot approach. That is, each local estimate is independently obtained, without a spatial regularization employed in 2-D tomography inversions. The fluctuations are likely controlled by variable wavefield and SNR characteristics, and should thus not be modelled using complicated and geophysically difficult to reconcile $v_S(z)$ distributions.

Fig. 2(b) illustrates the most probable model (blue solid line) estimated from the best 500 models, their weighted average (orange solid line) as well as the probability of observing a shear-wave velocity value at each depth (shading). The probability of observing an interface at each depth interval is shown in Fig. 2(c), and the corresponding shear-wave sensitivity kernels for periods between 20 and 200 s are summarized in Fig. 2(d). Fig. S1 collects more examples from stations located in the Alps and surrounding areas.

For the first 10 km the v_S is fixed and the interface probability equals unity at all locations because we use the A. Nouibat *et al.* (2023) model with no exploration. Below 10 km we choose to work with the average of the 500 best-fitting models. While a synthetic dispersion curve computed from this ensemble provides a good estimate of the observed data, the variability among these models—evident in both the v_S and interface probability distributions—highlights the inherent non-uniqueness of the Rayleigh-wave dispersion inversion. In particular, the v_S probability distribution indicated by the shading in Fig. 2(b) and related panels in Fig. S1 shows an average ±0.3 km s^{-1} variability around the average, and the distributions tends to be broader at depths where interfaces are inferred. The interface probability often shows a gradient with depth, especially in the deeper parts of the model, which leads to velocity transitions in the final model compared to sharp discontinuities. This behaviour is controlled by the characteristics of the sensitivity kernels, which indicate a better resolution closer to the surface and a comparatively poor resolution of deeper interfaces.

4 RESULTS

4.1 Phase velocity images

Fig. 3(a) shows phase velocity images for the periods between 20 and 150 s, together with the corresponding RSS and standard error distributions in Figs 3(b) and (c), respectively, that are obtained with the tools described in Section 2. The median-filtered phase velocity images are shown using the Voronoi tessellation in Fig. 3(d) and on a smoothly interpolated grid in Fig. 4(a) using the discretization of E.D. Kästle *et al.* (2018). This facilitates the comparison with the results of E.D. Kästle *et al.* (2018) (Fig. 4b) and A. El-Sharkawy *et al.* (2020) (Fig. 4c) that are obtained using ambient-noise and earthquake, and earthquake data, respectively.

The 20 s image resolves lateral variations of the phase velocity in the lower crust and at Moho depth. On average, the velocity at each location is estimated using data within a radius of 100 km

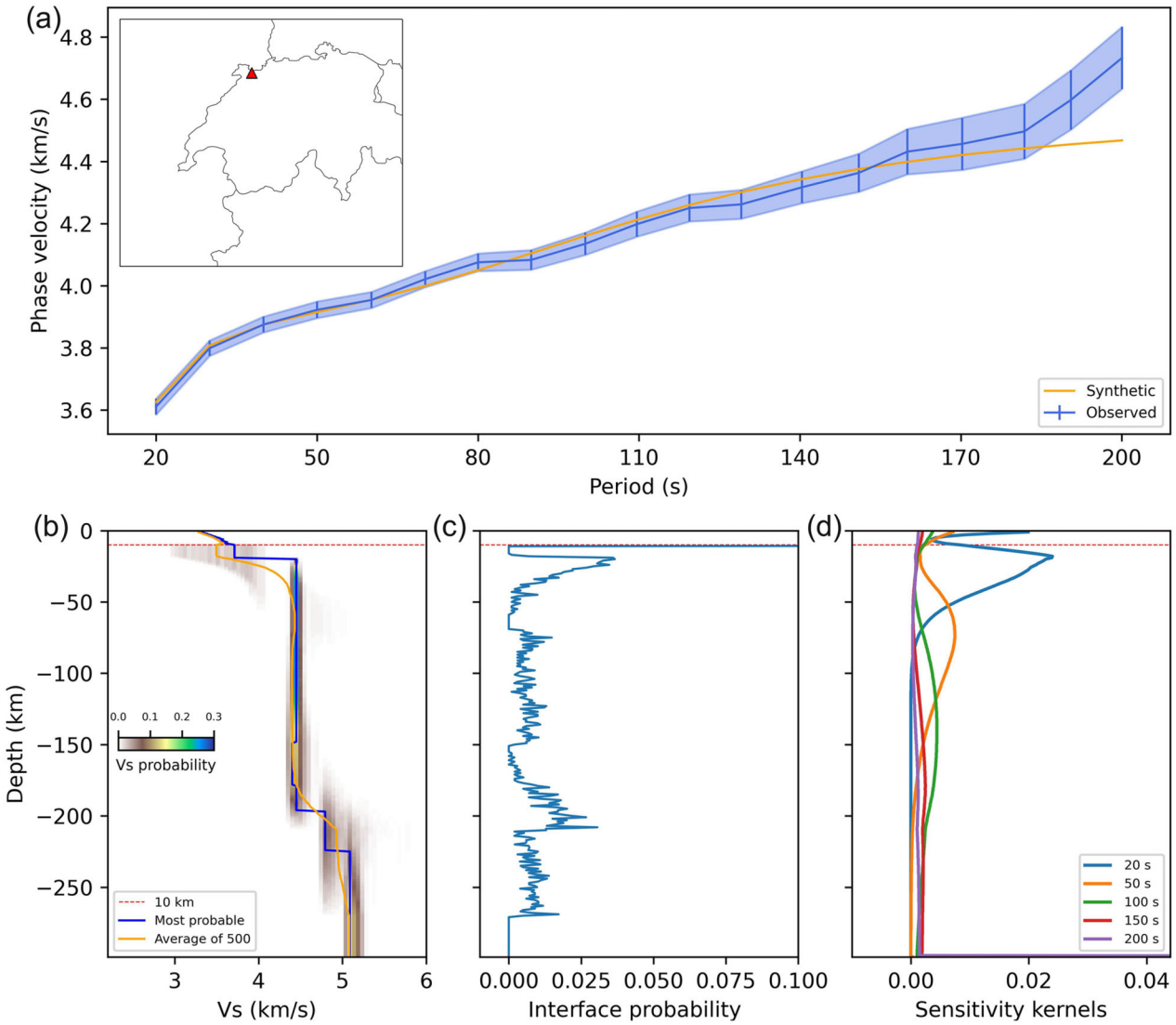

Figure 2. Phase velocity dispersion and shear-wave velocity inversion at station CH.BOURR in North-Western Switzerland. (a) The observed dispersion curve is sampled between periods of 20 and 200 s with intervals of 10 s. The error bars are the uncertainty estimates computed from eq. (4). The orange line indicates the synthetic dispersion curve average of the 500 best fit models. (b) The most probable shear-wave velocity model (blue) and the average of the 500 best fit models (orange) together with the associated probability distributions. (c) Shear-wave velocity interface probability obtained from the 500 best-fitting models. (d) Sensitivity kernels associated with the 500 best-fitting models average.

indicated by the black scale in Fig. 3(a). The coherent low velocities below the Apennines and the Alps indicate well resolved large-scale crustal thickness variations (Fig. 3a). The method resolves known geological features on a smaller scale equally well. The intermediate-velocity area in the Western Alps can be associated with the Ivrea geophysical body, which is interpreted as a slice of the Adriatic mantle found at crustal depths (e.g. A. Nicolas *et al.* 1990). This and the associated interpolated 20 s phase velocity image (Fig. 4a) compares well with the results of E.D. Kästle *et al.* (2018) (Fig. 4b). The observed small-scale discrepancies are likely controlled by different data pre-processing choices and different method sensitivities. At 50 s period (Fig. S2) many imaged large-scale features including the low velocities to the West of the Alps and the high velocities in the Eastern Alps are consistent with the results of E.D. Kästle *et al.* (2018) and A. El-Sharkawy *et al.* (2020) (Figs S3 and S4). Differences to the tomographic references such as the observed high velocities along the Italian Peninsula including the Apennines are likely influenced by the array shape and the incomplete azimuthal coverage together with the average 300 km data range.

In the 100 s phase velocity image (Fig. 3a) the N-S trending bands of alternating high and low velocities do not correlate with known tectonic structure. We hypothesize that this anomaly is connected to biasing wavefield effects that require further analysis for mitigation. We emphasize, however, that this inconsistency does not appear to significantly affect the inversion for the shear-wave structure discussed in the next section. As a result, the 100 s images (Figs 3a and 4a) exhibit considerable differences to the results of E.D. Kästle *et al.* (2018) and A. El-Sharkawy *et al.* (2020) (Figs 4b and c). At longer periods, the 150 s images show again more consistent velocity variations (Fig. 4) compared to the two tomographic images. This refers to

Table 1. The sketch to the left illustrates the model space parameters and their exploration ranges detailed to the right. This configuration is used for the vertical shear-wave velocity profile inversion discussed in Section 3.

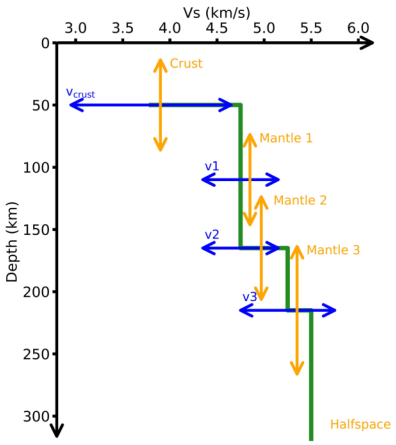

Layer	Interface depth (km)	v_S (km/s)
Sediments	0−10	Nouibat et al. (2023)
Crust	10−90	2.9−4.7
Mantle 1	70−150	4.3−5.2
Mantle 2	120−210	4.3−5.2
Mantle 3	160−270	4.7−5.8
Halfspace	300−∞	5.0−6.0

the low velocities to the West of the Alps in the Southeast corner of France and the large high-velocity area that covers Northern Italy, Western Austria and Southwestern Germany. Other areas of consistent spatial velocity variations include the low velocities in Eastern Austria and South-Eastern Germany in contrast to the high velocities in the Czech Republic. The focal spot velocity images resolve the low velocities below the Apennines in central Italy that is also evident in the images obtained by E.D. Kästle *et al.* (2018) and A. El-Sharkawy *et al.* (2020) (Figs 4b and c). The similar spatial velocity variation resolved at 150 s across the Italian Peninsula compared to the tomographic references indicates that the anisotropic model yields good results for focal spots that are spatially not fully reconstructed. At 150 s period a velocity contrast of 0.3 km s^{-1} across a 230 km distance in Southern Germany is imaged using a data distance range of $r_{\text{fit}} = 975$ km. A mean wavelength of $\lambda_{\text{mean}} = 650$ km corresponds to the resolution of a velocity variation on a scale of $0.35\lambda_{\text{mean}}$. This indicates subwavelength imaging (B. Giammarinaro *et al.* 2024) supported by the high station density compared to the wavelength.

The 200 s image (Figs S2 and S3) recovers again the low velocities to the West of the Alps which are also imaged by A. El-Sharkawy *et al.* (2020). This feature shows a larger difference in the focal spot phase velocity estimates, and this trend of larger focal spot based amplitude variations is also observed in the 150 s images. This difference in contrast reflects the different imaging algorithms. In seismic tomography, a regularization is commonly adopted to stabilize the solution of the inverse problem that controls the lateral resolution. In focal spot imaging, the data range affects the velocity contrast, but in the range between 1λ and 2λ the impact on the obtained images is comparatively weak (C. Tsarsitalidou *et al.* 2024). At these long periods, an overestimation of the velocity associated with focal spot imaging is probably due to the bias of the *P*-wave energy from the global reverberations manifesting on the ZZ-component cross-correlations (C. Tsarsitalidou *et al.* 2024).

The RSS and standard error images (Figs 3b and c) inform about the spatially variable quality of the obtained solutions. The distributions at 20 s indicate a good resolution in the Alpine region and in central Italy. In contrast, the northern section of the Apennines exhibits comparatively high values. These variations result from the interaction of the incident wavefield with the local structure and can thus contain complementary structural information. The images at longer periods are characterized by a general N-S trend controlled by the station configuration. Note the larger errors along the Cifalps profile in the Western Alps associated with the limited acquisition time. We emphasize that the access to local uncertainty estimates indicated in the dispersion curves (Figs 2a and S1) are an advantageous feature of the focal spot approach compared to tomography.

We analyse the correlation of the velocity estimates from the three imaging results using scatter diagrams and estimate the Pearson correlation coefficient PCC for all periods (Fig. 5). The PCC is related to the covariance between the elements of two data sets scaled by their standard deviations, and it provides here a measure of the linear correlation between two velocity data sets. The results support our findings based on the comparison of the phase velocity images in Fig. 4. The PCC between our focal spot imaging and the two tomography results is positive up to 60 s. Almost neutral PCC values at 100 s indicate uncorrelated images associated with the banded velocity variations (Fig. 3a), but the correlation is again positive at 150 and 200 s. The comparison of the two tomography results shows positive correlation for all periods (Fig. 5c). We point out that E.D. Kästle *et al.* (2018) and A. El-Sharkawy *et al.* (2020) apply the same method to similar data sets for their solutions above 75 s. Interestingly, the PCC trend shows the same behaviour as for the focal spot data with the same PCC minimum at 100 s. The good correlation between the focal spot and the tomography results at short periods is also illustrated by the scatter plots. At longer periods, the horizontally elongated clusters in Figs 5(a) and (b) reflect the larger contrast in the focal spot images. The average location below the parity line reflects the overestimation from the focal spot analysis.

4.2 The 3-D shear-wave velocity model

We invert the dispersion curves estimated at every station location to compile a 3-D v_S model. Fig. 6 shows the resulting v_S images at different depths between 15 and 80 km. As said, these are averages of the 500 best-fitting models. At each depth, we apply the spatial median filter discussed for the phase velocity images (Section 2.4).

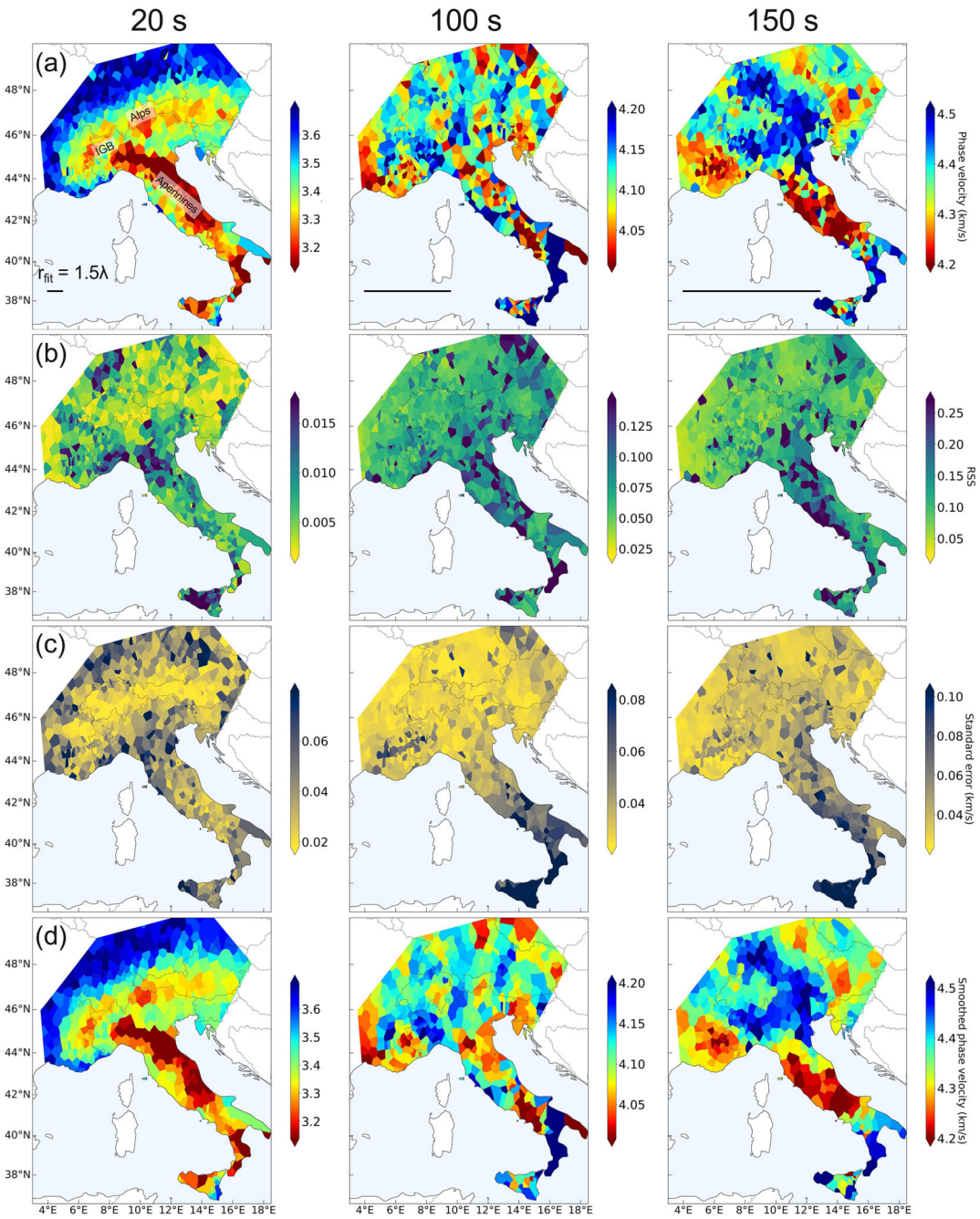

Figure 3. (a) Focal spot Rayleigh-wave phase velocity images for the periods 20, 100 and 150 s estimated with the anisotropic regression described in Section 2.3. The black scale bar in the lower left shows the average data range used for each image. (b) RSS estimates obtained from the misfit between the focal spot data and the anisotropic Bessel-function model. (c) Standard error computed from eq. (4). The visible line array across the French-Italian border is the Cifalps line. (d) Smoothed versions of the phase velocity images in panel (a) after application of a spatial median filter. IGB: Ivrea Geophysical Body.

The 15 km depth section features low velocities beneath the Alps and the Apennines in the v_S range around 3.4 and 3.2 km s^{-1}, respectively, which indicates the lower velocities of the Adriatic crust compared to the European crust. We find that our v_S model at this depth is compatible with independently obtained results (A. Nouibat *et al.* 2022), even in areas of poor azimuthal station coverage such as Southern Italy and Sicily.

The v_S features in the 30 km depth section image can be associated with the Moho topography. The roots of the Alps and Apennines can be observed at this depth with v_S values lower than their surrounding areas. The roots correspond to v_S values of ∼3.5 km s^{-1} associated with the lower crust, in contrast to the ∼4 km s^{-1} upper-mantle velocities around it, which is compatible with tomographic imaging results (I. Molinari *et al.* 2015; Y. Lu *et al.* 2018; A. Nouibat *et al.* 2022).

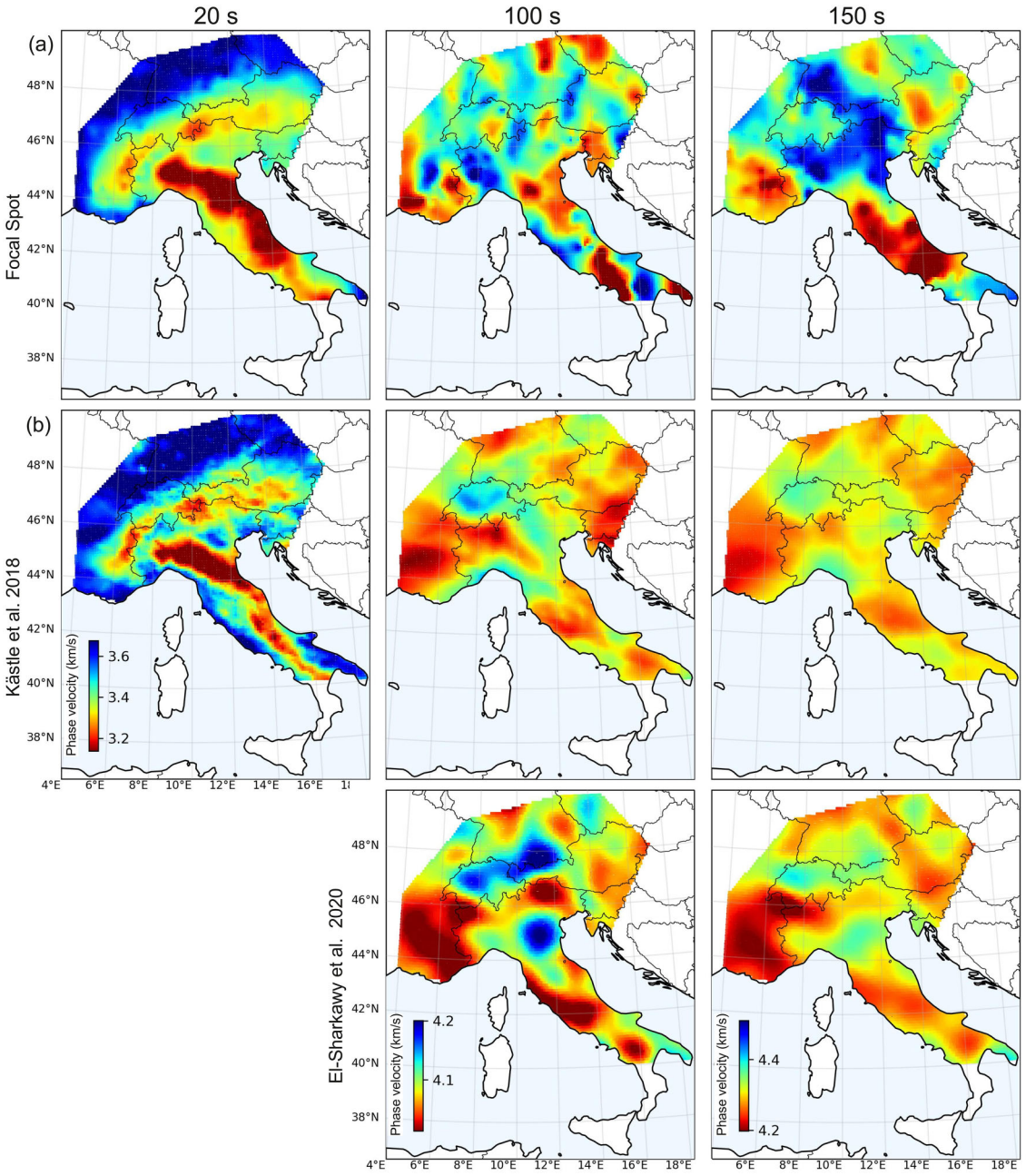

Figure 4. Phase velocity images from (a) the focal spot method, (b) E.D. Kästle *et al.* (2018) and (c) A. El-Sharkawy *et al.* (2020). The images in panel (a) are the interpolated version of the images in Fig. 3(d). The images of the three studies share the same colourbar shown in the bottom panels.

At 60 km depth we observe a spatial distribution of v_S variations that is similar to the pattern reported by A. Nouibat *et al.* (2022). However, the absolute v_S values in our model tend to be slightly higher. At this depth, the Apennines display higher v_S values than the Alps, which can be associated with the Adriatic mantle and which suggests a thinner crust beneath the Apennines. The region of the Southern Rhône Valley exhibits the lowest v_S value estimates (<4.4 km s^{-1}) in the imaged area. We find again that our model tends to overestimate the absolute v_S values in comparison to A. Nouibat *et al.* (2022), which is linked to the overestimation of the phase velocity discussed in Section 4.1.

At 80 km depth the v_S image is overall compatible with the model of E.D. Kästle *et al.* (2018) (their fig. 12), as our image also features the high velocities below the Apennines and the Alps. The two results can differ, however, at smaller scales, which again reflects the sensitivities to the different processing chains and imaging techniques.

We compare deeper sections of the model at 100, 145 and 205 km to the results of E.D. Kästle *et al.* (2025) (Fig. S5). At 100 km depth we observe similar spatial v_S distributions including the high v_S values along the North Apenninic slab in contrast to the low velocities in North-Eastern Italy, and the Adriatic Front characterized by a low-to-high velocity contrast. A consistent feature in all three depth sections obtained with both models is the area of low v_S velocities ranging across Eastern France, Southern Germany and Northern Austria. These consistencies at large depths support the effectiveness of the v_S inversion based on Rayleigh-wave focal spot dispersion estimates.

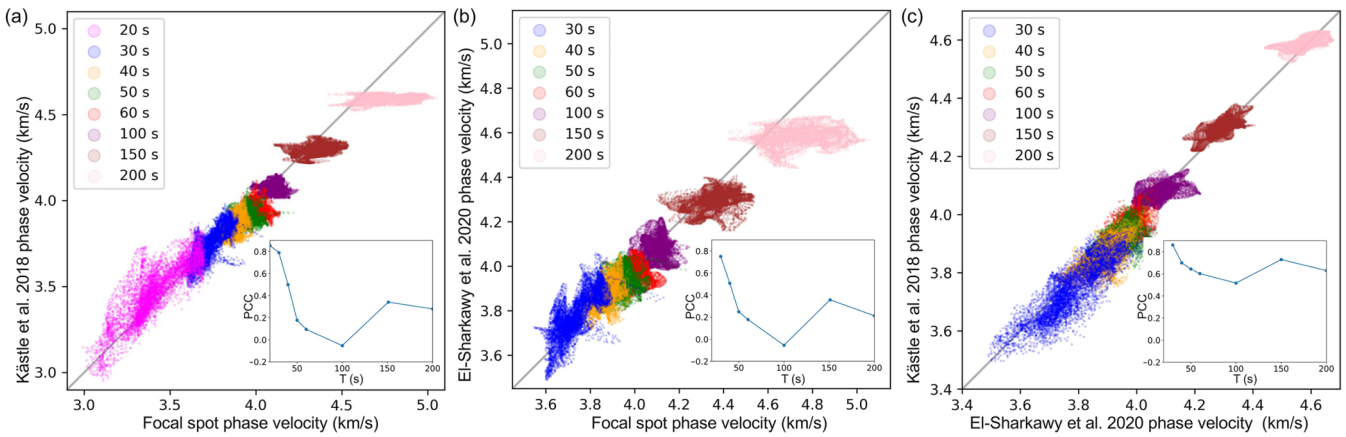

Figure 5. Scatter plots for comparison of the phase velocity estimates. (a) Data from the focal spot method and from E.D. Kästle *et al.* (2018) for periods 20 to 200 s. (b) Data from the focal spot method and from A. El-Sharkawy *et al.* (2020) for periods 30 to 200 s. (c) Data from E.D. Kästle *et al.* (2018) and from A. El-Sharkawy *et al.* (2020) for periods 30 to 200 s. The period-dependent Pearson correlation coefficient PCC is shown in the insets.

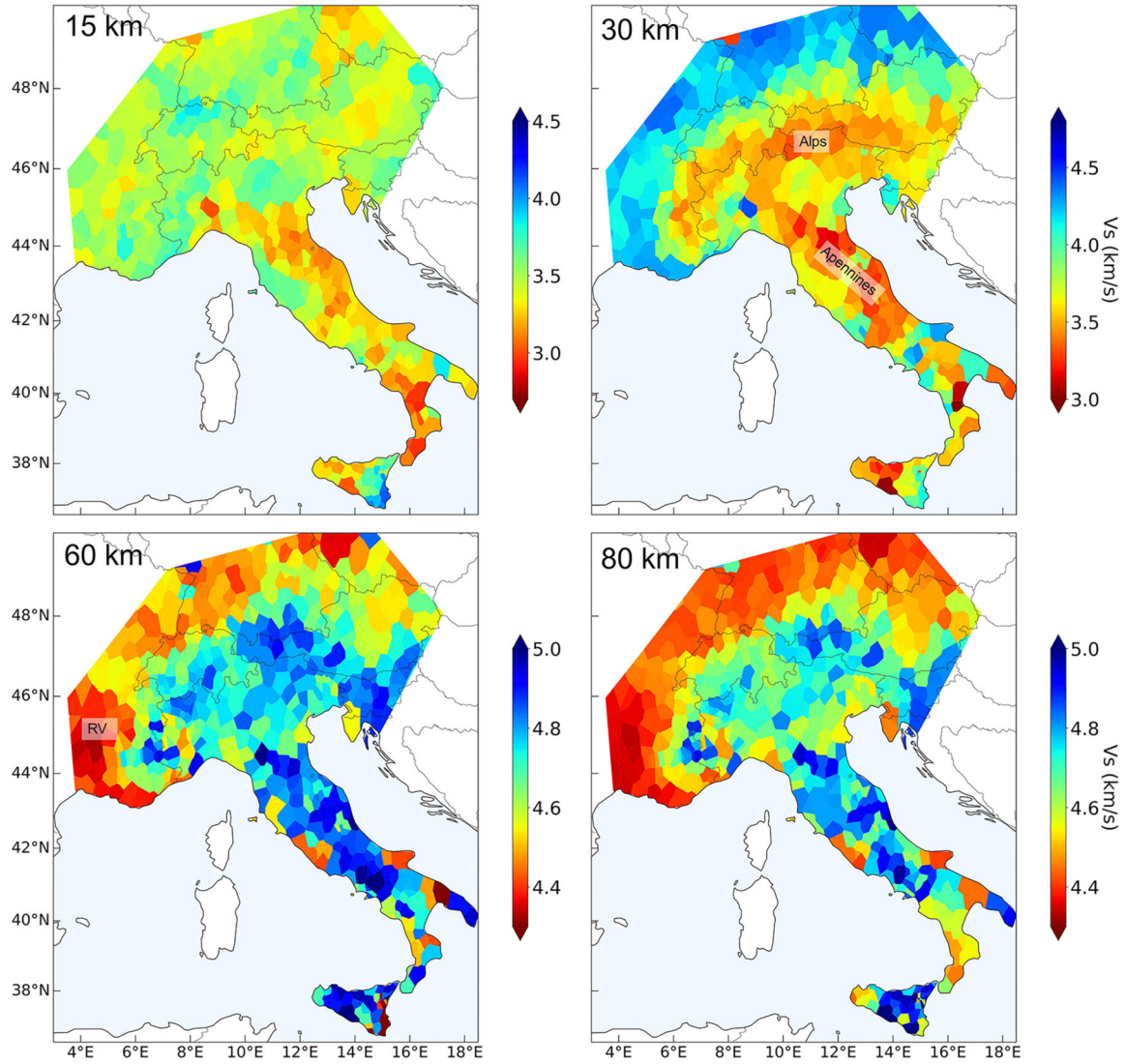

Figure 6. Depth sections of the shear-wave velocity v_S model at 15, 30, 60 and 80 km. The used v_S model is the average of the 500 best-fitting models. We apply a median filter at each station location that replaces each v_S value with the median of the local v_S estimate and its two nearest neighbours. RV: Rhône Valley.

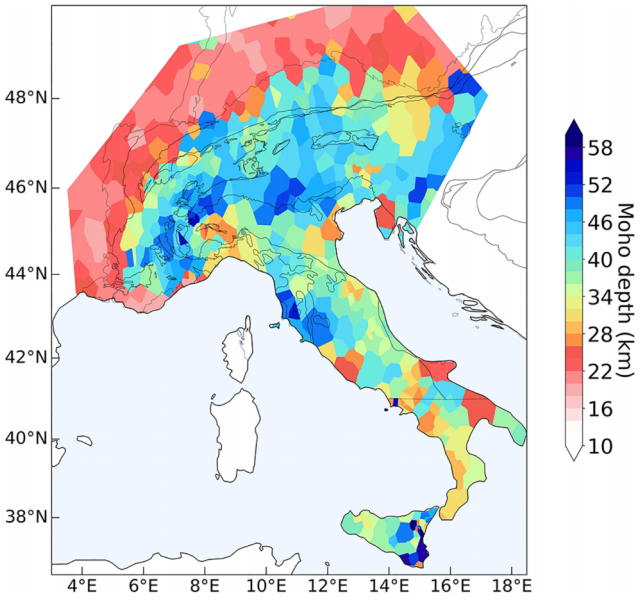

Figure 7. An image of the Moho depth estimate obtained from the steepest gradient of the v_S model that is the average over the 500 best-fitting models. At each station location the indicated Moho depth is the median value of the local Moho depth estimate and its two nearest neighbours. The colour range follows A. Nouibat *et al.* (2023) for comparison. The boundaries of the tectonic provinces in the Alps are from S. Schmid *et al.* (2004) and M.R. Handy *et al.* (2019).

4.3 An image of the Moho depth

We conclude this section by compiling an image of the focal spot based Moho depth variation (Fig. 7). We adopt the definition of the transitional Moho used by Y. Lu *et al.* (2018) and identify the Moho as the depth of a strong v_S gradient between 20 and 60 km depth, which is the known Moho depth range of the Alps, the Apennines and surrounding areas. We apply this definition because our v_S model, averaged over the best 500 solutions, exhibits gradual transitions with depth, and not discrete interfaces.

While high-resolution imaging of the Moho structure is important for understanding the complex tectonic processes beneath the Alps, we consider here an exploratory approach and focus on first-order observations to evaluate the extent to which focal spot dispersion data can resolve major structural features. We find that the broader characteristics of the Moho image in Fig. 7 are compatible with previously discussed Moho topographies (e.g. fig. 9 in A. Nouibat *et al.* 2023) North of 43° N. Starting from the North, the European Moho is found at the red indicated depths between 18 and 24 km. Below the central parts of the Alps the crustal thickness varies between 40 and 50 km indicated in blue. In between the more yellow and green shades indicate the ∼34 km deep Moho below the Molasse basin to the North of the Alps, which is again consistent with the model of A. Nouibat *et al.* (2023). Interestingly, our approach resolves the location of the Ivrea Geophysical Body (IGB) in North-Western Italy towards the border with France. Its 30 km surface is deeper compared to the results by A. Nouibat *et al.* (2023), however, it can be robustly identified in contrast to the surrounding Moho depth of the Western Alps at approximately 50 km. This IGB signal extends over only two to three pixels in the focal spot image. Together with the accurately resolved location, this imaging result demonstrates that phase velocity data estimated with the focal spot technique yield meaningful shear-wave velocity profiles.

The inversion for two instead of one v_S interfaces between 10 and 100 km yields a shear-wave structure that resolves the top of the IGB at a Moho depth of 22 km (Fig. S6). However, in other regions such as the Alpine foreland this approach yields depth estimates that are not compatible with other Moho images (I. Molinari *et al.* 2015; Y. Lu *et al.* 2020; A. Nouibat *et al.* 2023). An optimized v_S model space parametrization can potentially improve the structural resolution in this area. Our Moho image is a proxy controlled by the decreasing depth sensitivity of the long period surface waves, and by algorithmic choices associated with the v_S inversion and the Moho definition. Results from inversions using Moho reflections can thus differ, however, the general compatibility of the obtained image in comparison with tomographic results including the resolution of the complex IGB area suggest the effectiveness of structural focal spot imaging.

5 DISCUSSION AND CONCLUSIONS

The focal spot is the zero lag time amplitude distribution of ambient-noise cross-correlations and thus the time domain spatial autocorrelation field (V.C. Tsai & M.P. Moschetti 2010). We parametrize focal spots with models developed in SPAC theory (K. Aki 1957; M.M. Haney *et al.* 2012) to estimate fundamental-mode Rayleigh-wave phase velocity. After the widespread utilization of the frequency-domain SPAC technique and its derivatives for near-surface applications using small, tuned arrays and the extension of the SPAC approach to invert for spatial velocity variations (G. Ekström *et al.* 2009; G. Ekström 2014), the focal spot technique provides an elegant, complementary approach to seismic surface wave imaging. In contrast to tomographic inversion frameworks, focal spot images are compiled with no explicit regularization because the images are based on local velocity estimates using data from distances on the order of 1λ. This approach yields local frequency-dependent uncertainty estimates that reflect data quality and the interaction of the ambient-noise wavefield with the local structure (G. Hillers *et al.* 2016; C. Tsarsitalidou *et al.* 2024), which can be used in the inversion of the observed dispersion. Limiting the analysis to short distances enhances the vertical and lateral resolution of dense array surface wave imaging. Vertically, because long period waves with correspondingly larger depth sensitivity to deeper Earth structure can be studied (C. Tsarsitalidou *et al.* 2024); and laterally, because the data quality and hence the distance range controls the lateral resolution (B. Giammarinaro *et al.* 2024).

In this work, we estimate Rayleigh-wave phase velocities across the European Alps and surrounding regions using ZZ-component regression models in the 20 to 200 s period range. Our work extends previous spatial autocorrelation imaging approaches (G. Ekström 2014; G. Hillers *et al.* 2016; C. Tsarsitalidou *et al.* 2024) by implementing a model that parametrizes the anisotropic background illumination (M.M. Haney *et al.* 2012). The model accounts for the strong anisotropic incidence of the wavefield along the SW-NE direction (Fig. 1). The spatial sampling is heterogeneous in the otherwise well-covered Alpine region compared to the incomplete azimuthal coverage in the Italian Peninsula.

We obtain images of the Rayleigh-wave phase velocity together with distributions of the residual sum of squares and the standard-error for the 20 to 200 s period range (Fig. 3), that

are used together to assess the results. At shorter periods the solution quality reflects the geological structure. At longer periods the observations suggest that the distance and azimuth-dependent sampling of the autocorrelation fields relative to the direction of incidence influences the obtained solutions. The velocity uncertainties tend to be larger in areas with limited azimuthal coverage, that is, in the Italian peninsula and Sicily, and high RSS values in central Italy are oriented perpendicular to the incidence direction. Despite the limited synchronicity of the west–east oriented line arrays Cifalps (L. Zhao *et al.* 2016) and Cifalps2 (L. Zhao *et al.* 2018) with the surrounding stations, the line array shapes do not dominate the phase velocity images, but the resulting lower SNR controls the higher standard errors along the Cifalps line. These lines are parallel to the wavefield incidence, in contrast to the north–south trending EASI network (AlpArray Seismic Network 2014) that we sorted out because of the obtained low-quality results. In addition to these systematic effects that are controlled by the configuration, the phase velocities, RSS and standard error distributions exhibit small-scale artefacts or fluctuations that are not compatible with the results in the neighbouring locations. These can be attributed to data quality related local effects associated with installation or coupling, or local noise sources or scatterers (G. Hillers *et al.* 2016) that all degrade the compatibility of the amplitude distributions with the employed 2-D parametrization.

In this work, we mitigate the influence of these fluctuations by applying a median filter to the original imaging results. The scale of these fluctuations is smaller than the few-pixels wide features in the 100 s phase velocity images, but these images are characterized by an overall limited consistency between the three different imaging studies (Figs 3 and 4). This suggests an overall poor resolution that is governed by the original wavefield properties in this period range, in contrast to the again more consistent results at 150 s (Figs 3 and 4). As for ambient noise tomography, a consistent, synchronous data acquisition supports coherent imaging results. Generally, the results from our employed distance and direction-dependent 2-D SPAC model are expected to be more robust for anisotropic incidence compared to the standard 1-D model when the station configuration does not support full azimuthal focal spot sampling. Our analysis shows that the effects of heterogeneous noise distributions and irregular station density in relation to the sampled focal spot segments can influence the velocity and quality control estimates. However, the sensitivities, trade-offs and limits on the lateral resolution associated with these factors cannot be separated based on the available observations and require a systematic exploration to inform effective processing improvements. Alternative enhancement strategies can focus on the data quality based selection of focal spot samples for the regression, and correlating data from time periods or seasons during which more coherent surface wave energy is excited in a way to use less data more efficiently (e.g. C. Esteve *et al.* 2025).

We invert the local focal spot dispersion curves using the Neighbourhood Algorithm (M. Sambridge 1999) to obtain a pseudo 3-D shear-wave velocity v_S model. The investigation focus of this study (V.C. Tsai 2023) is the assessment of the compatibility of the v_S estimates obtained from the inversion of the focal spot dispersion curves with tomographic images. Overall, the comparison with regional ambient-noise and earthquake tomography studies at short and long periods demonstrates that focal spot imaging is sensitive to the elastic Earth structure in this complex tectonic plate boundary region. The resolved features from our v_S model constrained between 10 and 200 km depth are compatible with the results in reference tomographic studies (I. Molinari *et al.* 2015; Y. Lu *et al.* 2018; A. Nouibat *et al.* 2022; E.D. Kästle *et al.* 2025). We mention the imaging of the two major mountain belts, the Alps and Apennines, that are resolved as low-velocity regions at short periods and shallow depths and as high-velocity regions at longer periods and greater depths, and the resolution of the complex area around the Ivrea Geophysical Body. Variations in the absolute velocities and depth estimates of interfaces obtained with the individual approaches can help to evaluate the trade-offs and sensitivities associated with the different data types and analysis techniques.

Similar to the original autocorrelation approach the results imply that a velocity profile can be constrained under an array to depths that are not accessible to propagating surface waves analysed by tomography, which highlights the valuable contribution of focal spot lithospheric imaging. Dense array focal spot imaging is an effective complementary technique to ambient noise tomography for the construction of relevant v_S models.

ACKNOWLEDGMENTS

We thank M. Campillo, L. Seydoux and Y. Lu for helpful discussions. We thank E. Kästle and A. El-Sharkawy for providing the phase velocity maps of their studies (E.D. Kästle *et al.* 2018; A. El-Sharkawy *et al.* 2020). We thank the editor A. Obermann, and E. Kästle and an anonymous reviewer for comments that helped to improve this manuscript. We acknowledge the University of Helsinki IT4Science team for their support, and the computational and data storage resources of the Finnish Grid and Cloud Infrastructure (FGCI, urn:nbn:fi:research-infras-2016072533). This work was supported by the Research Council of Finland (Flagship of Advanced Mathematics for Sensing Imaging and Modeling grant 359182 and grant 322421). CT acknowledges support from the Finnish Academy of Science and Letters.

SUPPORTING INFORMATION

Supplementary data are available at *GJIRAS* online.

Please note: Oxford University Press is not responsible for the content or functionality of any supporting materials supplied by the authors. Any queries (other than missing material) should be directed to the corresponding author for the paper.

DATA AVAILABILITY

We used continuous records from the AlpArray temporary network (AlpArray Seismic Network 2014) and from stations associated with the permanent seismic networks BW (Department of Earth and Environmental Sciences, Geophysical Observatory, University of Munchen 2001), CH (Swiss Seismological Service (SED) 1983), CR (University of Zagreb 2001), CZ (Charles University in Prague (Czech) 1973), FR (Epos-France Seismological Data Centre 1962), GE (GEOFON Data Centre 1993), GR (Federal Institute for Geosciences and Natural Resources 1976), GU (University of Genoa 1967), IV (Istituto Nazionale di Geofisica e Vulcanologia (INGV) 2005), MN (MedNet Project Partner Institutions 1990), NI (Istituto Nazionale di Oceanografia e di Geofisica Sperimentale & University of Trieste 2002), OE (ZAMG—Zentralanstalt für Meterologie und Geodynamik 1987), OX (Istituto Nazionale di Oceanografia e di Geofisica Sperimentale—OGS 2016), SL (Slovenian Environment Agency 1990), XT (L.

Zhao *et al.* 2018), and YP (L. Zhao *et al.* 2016). The correlation functions database is available on the EasyData.earth repository (L. Stehly 2025). The software used to process the continuous data can be accessed from P. Boué & L. Stehly (2022). The Python code for estimating the phase velocity distributions can be obtained from B. Giammarinaro & G. Hillers (2022). The sensitivity kernels were computed using the solution of K. Luu (2021).

REFERENCES

Aki, K., 1957. Space and time spectra of stationary stochastic waves, with special reference to microtremors, *Bull. Earthq. Res. Inst. Univ. Tokyo,* **35,** 415–457.

AlpArray Seismic Network, 2014. Eastern Alpine Seismic Investigation (EASI) - AlpArray Complimentary Experiment.AlpArray Working Group. 10.12686/alparray/xt_2014.

AlpArray Seismic Network, 2015. AlpArray Seismic Network (AASN) temporary component. AlpArray Working Group. 10.12686/alparray/z3_2015.

Ardhuin, F., Gualtieri, L. & Stutzmann, E., 2015. How ocean waves rock the Earth: Two mechanisms explain microseisms with periods 3 to 300 s, *Geophys. Res. Lett.,* **42**(3), 765–772.

Arrowsmith, S.J., Trugman, D.T., MacCarthy, J., Bergen, K.J., Lumley, D. & Magnani, M.B., 2022. Big Data Seismology, *Rev. Geophys.,* **60**(2)..

Asten, M.W. & Hayashi, K., 2018. Application of the spatial autocorrelation method for shear-wave velocity studies using ambient noise, *Surv. Geophys.,* **39,** 633–659.

Aster, R.C., Borchers, B. & Thurber, C.H., 2013. Chapter nine - nonlinear regression, *Parameter Estimation and Inverse Problems, 2 edn.,* pp. 217–238, eds Aster, R.C., Borchers, B. & Thurber, X.H., Academic Press, Boston.

Bensen, G.D., Ritzwoller, M.H., Barmin, M.P., Levshin, A.L., Lin, F., Moschetti, M.P., Shapiro, N.M. & Yang, Y., 2007. Processing seismic ambient noise data to obtain reliable broad-band surface wave dispersion measurements, *Geophys. J. Int.,* **169**(3), 1239–1260.

Blondel, T., Chaput, J., Derode, A., Campillo, M. & Aubry, A., 2018. Matrix approach of seismic imaging: application to the Erebus volcano, Antarctica, *J. geophys. Res.: Solid Earth,* **123**(12), 10 936–10 950.

Boué, P. & Stehly, L., 2022. Pycorr (v1.0) [Software]. Zenodo. 10.5281/zenodo.6793401.

Boué, P., Poli, P., Campillo, M. & Roux, P., 2014. Reverberations, coda waves and ambient noise: Correlations at the global scale and retrieval of the deep phases, *Earth planet. Sci. Lett.,* **391,** 137–145.

Brum, J., Catheline, S., Benech, N. & Negreira, C., 2015. Quantitative shear elasticity imaging from a complex elastic wavefield in soft solids with application to passive elastography, *IEEE Trans. Ultrason. Ferroelectr. Frequency Control,* **62**(4), 673–685.

Campillo, M. & Roux, P., 2015. P. 1.12 Crust and lithospheric structure—seismic imaging and monitoring with ambient noise correlations, in *Treatise on Geophysics, 2nd edn.,* pp. 391–417, ed. Schubert, G., Elsevier.

Catheline, S., Souchon, R., Rupin, M., Brum, J., Dinh, A.H. & Chapelon, J.Y., 2013. Tomography from diffuse waves: passive shear wave imaging using low frame rate scanners, *Appl. Phys. Lett.,* **103**(1), 014101.

Charles University in Prague (Czech), Institute of Geonics, Institute of Geophysics, Academy of Sciences of the Czech Republic, Institute of Physics of the Earth Masaryk University (Czech)& Institute of Rock Structure and Mechanics, 1973. Czech regional seismic network.International Federation of Digital Seismograph Networks. 10.7914/SN/CZ.

Cox, H., 1973. Spatial correlation in arbitrary noise fields with application to ambient sea noise, *J. acoust. Soc. Am.,* **54**(5), 1289–1301.

de Ridder, S.A.L. & Biondi, B.L., 2015. Near-surface Scholte wave velocities at Ekofisk from short noise recordings by seismic noise gradiometry, *Geophys. Res. Lett.,* **42**(17), 7031–7038.

Deen, M., Stutzmann, E. & Ardhuin, F., 2018. The Earth's Hum Variations From a Global Model and Seismic Recordings Around the Indian Ocean, *Geochem. Geophys. Geosyst.,* **19**..

Department of Earth and Environmental Sciences, Geophysical Observatory, University of Munchen, 2001. BayernNetz. International Federation of Digital Seismograph Networks. 10.7914/SN/BW.

Derode, A., Larose, E., Campillo, M. & Fink, M., 2003a. How to estimate the Green's function of a heterogeneous medium between two passive sensors? Application to acoustic waves, *Appl. Phys. Lett.,* **83**(15), 3054–3056.

Derode, A., Larose, E., Tanter, M., de Rosny, J., Tourin, A., Campillo, M. & Fink, M., 2003b. Recovering the Green's function from field-field correlations in an open scattering medium (L), *J. acoust. Soc. Am.,* **113**(6), 2973–2976.

Draganov, D., Campman, X., Thorbecke, J., Verdel, A. & Wapenaar, K., 2009. Reflection images from ambient seismic noise, *Geophysics,* **74**(5), A63–A67.

Ekström, G., 2014. Love and Rayleigh phase-velocity maps, 5–40 s, of the western and central USA from USArray data, *Earth planet. Sci. Lett.,* **402,** 42–49.

Ekström, G., Abers, G.A. & Webb, S.C., 2009. Determination of surface-wave phase velocities across USArray from noise and Aki's spectral formulation, *Geophys. Res. Lett.,* **36**(18).

El-Sharkawy, A., Meier, T., Lebedev, S., Behrmann, J.H., Hamada, M., Cristiano, L., Weidle, C. & Köhn, D., 2020. The slab puzzle of the Alpine-Mediterranean Region: insights from a new, high-resolution, shear wave velocity model of the upper mantle, *Geochem. Geophys. Geosyst.,* **21**(8).

Epos-France Seismological Data Centre, 1962. Epos-France Broad-band network (RLBP) [Data set]. Epos-France. doi.org/10.15778/RESIF.FR.

Esteve, C., Lu, Y., Gosselin, J., Kramer, R., Aiman, Y. & Bokelmann, G., 2025. The seismic signature and geothermal potential of the Schwechat Depression in the Vienna Basin, Austria, from ambient noise tomography, *Geothermics,* **127,** 103211.

Federal Institute for Geosciences and Natural Resources, 1976. German Regional Seismic Network (GRSN). Bundesanstalt für Geowissenschaften und Rohstoffe. 10.25928/MBX6-HR74.

Fink, M., 1999. Time-reversed acoustics, *Sci. Am.,* **281**(5), 91–97.

Foti, S. *et al.*, 2018. Guidelines for the good practice of surface wave analysis: a product of the InterPACIFIC project, *Bull. Earthq. Eng.,* **16,** 2367–2420.

Galetti, E. & Curtis, A., 2012. Generalised receiver functions and seismic interferometry, *Tectonophysics,* **532–535,** 1–26.

GEOFON Data Centre, 1993. Geofon seismic network.GFZ Data Services. 10.14470/TR560404.

Giammarinaro, B. & Hillers, G., 2022. Resources for seismic surface wave focal spot imaging: numerical resolution experiments [Software]. University of Helsinki. 10.23729/61e3eefb-e7ce-44af-8fc3-01cac0bbba0d.

Giammarinaro, B., Tsarsitalidou, C., Hillers, G., de Rosny, J., Seydoux, L., Catheline, S., Campillo, M. & Roux, P., 2023. Seismic surface wave focal spot imaging: numerical resolution experiments, *Geophys. J. Int.,* **232,** 201–222.

Giammarinaro, B., Tsarsitalidou, C. & Hillers, G., 2024. Investigating the lateral resolution of the surface wave focal spot imaging technique using two-dimensional acoustic simulations, *C. R. Geosci.,* **356,** 41–57.

Handy, M.R., Giese, J., Schmid, S.M., Pleuger, J., Spakman, W., Onuzi, K. & Ustaszewski, K., 2019. Coupled Crust-Mantle Response to Slab Tearing, Bending, and Rollback Along the Dinaride-Hellenide Orogen, *Tectonics,* **38**(8), 2803–2828.

Haney, M.M., Mikesell, T.D., van Wijk, K. & Nakahara, H., 2012. Extension of the spatial autocorrelation (SPAC) method to mixed-component correlations of surface waves, *Geophys. J. Int.,* **191**(1), 189–206.

Herrmann, R.B., 2013. Computer programs in seismology: an evolving tool for instruction and research, *Seismol. Res. Lett.,* **84**(6), 1081–1088.

Hillers, G., Roux, P., Campillo, M. & Ben-Zion, Y., 2016. Focal spot imaging based on zero lag cross-correlation amplitude fields: Application

to dense array data at the San Jacinto fault zone, *J. geophys. Res.: Solid Earth,* **121**(11), 8048–8067.
Istituto Nazionale di Geofisica e Vulcanologia (INGV), 2005. Rete Sismica Nazionale (RSN).Istituto Nazionale di Geofisica e Vulcanologia (INGV). 10.13127/SD/X0FXNH7QFY.
Istituto Nazionale di Oceanografia e di Geofisica Sperimentale - OGS. 2016. North-east Italy seismic network. FDSN. 10.7914/SN/OX.
Istituto Nazionale di Oceanografia e di Geofisica Sperimentale& University of Trieste, 2002. North-east Italy broadband network & University of Trieste 2002. International Federation of Digital Seismograph Networks. 10.7914/SN/NI.
Kästle, E.D., El-Sharkawy, A., Boschi, L., Meier, T., Rosenberg, C., Bellahsen, N., Cristiano, L. & Weidle, C., 2018. Surface Wave Tomography of the Alps Using Ambient-Noise and Earthquake Phase Velocity Measurements, *J. geophys. Res.: Solid Earth,* **123**(2), 1770–1792.
Kästle, E.D., Paffrath, M. & El-Sharkawy, A.& the AlpArray and Swath-D working groups],, 2025. Alpine Crust and Mantle Structure From 3D Monte Carlo Surface- and Body-Wave Tomography, *J. geophys. Res.: Solid Earth,* **130**(2).
Lin, F.C. & Ritzwoller, M.H., 2011. Helmholtz surface wave tomography for isotropic and azimuthally anisotropic structure, *Geophys. J. Int.,* **186**(3), 1104–1120.
Lin, F.C., Ritzwoller, M.H. & Snieder, R., 2009. Eikonal tomography: surface wave tomography by phase front tracking across a regional broadband seismic array, *Geophys. J. Int.,* **177,** 1091–1110.
Lu, Y., Stehly, L., Paul, A. & Group, A.W., 2018. High-resolution surface wave tomography of the European crust and uppermost mantle from ambient seismic noise, *Geophys. J. Int.,* **214**(2), 1136–1150.
Lu, Y., Stehly, L., Brossier, R., Paul, A. & AlpArray Working Group, 2020. Imaging Alpine crust using ambient noise wave-equation tomography, *Geophys. J. Int.,* **222**(1), 69–85.
Luu, K., 2021. disba: Numba-accelerated computation of surface wave dispersion [Software], Zenodo.
MedNet Project Partner Institutions, 1990. Mediterranean Very Broadband Seismographic Network (MedNet) [Data set]. Available at: https://data.ingv.it/en/dataset/15#additional-metadata
Molinari, I., Verbeke, J., Boschi, L., Kissling, E. & Morelli, A., 2015. Italian and Alpine three-dimensional crustal structure imaged by ambient-noise surface-wave dispersion, *Geochem. Geophys. Geosyst.,* **16**(12), 4405–4421.
Nakahara, H., 2006. A systematic study of theoretical relations between spatial correlation and Green's function in one-, two- and three-dimensional random scalar wavefields, *Geophys. J. Int.,* **167**(3), 1097–1105.
Nakata, N., Chang, J.P., Lawrence, J.F. & Boué, P., 2015. Body wave extraction and tomography at long beach, California, with ambient-noise interferometry, *J. geophys. Res.: Solid Earth,* **120**(2), 1159–1173.
Nakata, N., Gualtieri, L. & Fichtner, A., 2019. *Seismic Ambient Noise*, Cambridge University Press.
Nicolas, A., Hirn, A., Nicolich, R. & Polino, R., 1990. Lithospheric wedging in the western Alps inferred from the ECORS-CROP traverse, *Geology,* **18**(7), 587–590.
Nouibat, A. *et al.*, 2022. Lithospheric transdimensional ambient-noise tomography of W-Europe: implications for crustal-scale geometry of the W-Alps, *Geophys. J. Int.,* **229**(2), 862–879.
Nouibat, A., Brossier, R., Stehly, L., Cao, J. & Paul, A.& Cifalps Team and AlpArray Working Group, 2023. Ambient-noise wave-equation tomography of the Alps and Ligurian-Provence Basin, *J. geophys. Res.: Solid Earth,* **128**(10).
Okada, H. & Suto, K., 2003. *The Microtremor Survey Method*, Society of Exploration Geophysicists.
Paul, A., Pedersen, H.A., Bodin, T., Kästle, E., Soergel, D., Alder, C., Lu, Y. & Nouibat, A., 2024. New developments in passive seismic imaging and monitoring methodological advances on seismic noise imaging in the Alpine area, *C. R. Géosci.,* **356,** 5--39.
Poli, P., Pedersen, H.A. & Campillo, M., 2012. Emergence of body waves from cross-correlation of short period seismic noise, *Geophys. J. Int.,* **188**(2), 549–558.
Sambridge, M., 1999. Geophysical inversion with a neighbourhood algorithm—I. Searching a parameter space, *Geophys. J. Int.,* **138**(2), 479–494.
Schmid, S., Fügenschuh, B., Kissling, E. & Schuster, R., 2004. Tectonic map and overall architecture of the Alpine orogen, *Eclogae Geolog. Helvetiae,* **97,** 93–117.
Seydoux, L., de Rosny, J. & Shapiro, N.M., 2017. Pre-processing ambient noise cross-correlations with equalizing the covariance matrix eigenspectrum, *Geophys. J. Int.,* **210**(3), 1432–1449.
Slovenian Environment Agency, 1990. Seismic network of the republic of Slovenia.International Federation of Digital Seismograph Networks. 10.7914/SN/SL.
Stehly, L., 2025. Vertical-vertical (ZZ) component cross-correlation database [Dataset], EasyData. 10.57932/8cd80a16-6623-4d4a-a088-5ad1a99a8f82.
Stehly, L., Fry, B., Campillo, M., Shapiro, N.M., Guilbert, J., Boschi, L. & Giardini, D., 2009. Tomography of the Alpine region from observations of seismic ambient noise, *Geophys. J. Int.,* **178**(1), 338–350.
Swiss Seismological Service (SED) at ETH Zurich, 1983. National Seismic Networks of Switzerland.ETH Zürich. 10.12686/SED/NETWORKS/CH.
Takagi, R., Nakahara, H., Kono, T. & Okada, T., 2014. Separating body and Rayleigh waves with cross terms of the cross-correlation tensor of ambient noise, *J. geophys. Res.: Solid Earth,* **119**(3).
Tsai, V.C., 2023. The Future of Earth imaging, *Seismol. Res. Lett.,* **94**(5), 2119–2128.
Tsai, V.C. & Moschetti, M.P., 2010. An explicit relationship between time-domain noise correlation and spatial autocorrelation (SPAC) results, *Geophys. J. Int.,* **182**(1), 454–460.
Tsarsitalidou, C., Giammarinaro, B., Hillers, G. & Boué, P., 2022. Anisotropic background illumination effects on focal spot imaging configurations with azimuthal asymmetry. AGU Fall Meeting 2022, Chicago, IL and online.
Tsarsitalidou, C., Hillers, G., Giammarinaro, B., Boué, P., Stehly, L. & Campillo, M., 2024. Long period Rayleigh wave focal spot imaging applied to USArray data, *J. geophys. Res.: Solid Earth,* **129**(5).
University of Genoa, 1967. Regional Seismic Network of North Western Italy. Available at: https://distav.unige.it/rsni/rete.php?lang=en
University of Zagreb, 2001. Croatian Seismograph Network. Available at: https://www.fdsn.org/networks/detail/CR/
Wang, J., Wu, G. & Chen, X., 2019. Frequency-Bessel transform method for effective imaging of higher-mode Rayleigh dispersion curves from ambient seismic noise data, *J. geophys. Res.: Solid Earth,* **124**(4), 3708–3723.
ZAMG - Zentralanstalt fur Meterologie und Geodynamik, 1987. Austrian seismic network.International Federation of Digital Seismograph Networks. 10.7914/SN/OE.
Zemzemi, C., Zorgani, A., Daunizeau, L., Belabhar, S., Souchon, R. & Catheline, S., 2020. Super-resolution limit of shear-wave elastography, *EPL (Europhys. Lett.),* **129**(3), 34002.
Zhao, K., Luo, Y. & Xie, J., 2017. Broad-band Rayleigh wave phase velocity maps (10–150 s) across the United States from ambient noise data, *Geophys. J. Int.,* **208**(2), 1265–1275.
Zhao, L., Paul, A. & Solarino, S.& RESIF, 2016. Seismic network YP: CIFALPS temporary experiment (China-Italy-France Alps seismic transect) [Data set]. Available at: https://data.ingv.it/dataset/741#additional-metadata
Zhao, L., Paul, A. & Solarino, S.& RESIF, 2018. Seismic network XT: CIFALPS-2 temporary experiment (China-Italy-France Alps seismic transect #2) [Data set]. Available at: https://data.ingv.it/en/dataset/924#additional-metadata